Icarus 273 (2016) 248–261

Contents lists available at ScienceDirect

Icarus

journal homepage: www.elsevier.com/locate/icarus

The Lassell massif—A silicic lunar volcano

J.W. Ashley[a, b, *], M.S. Robinson[a], J.D. Stopar[a], T.D. Glotch[c], B. Ray Hawke[d], C.H. van der Bogert[e], H. Hiesinger[e], S.J. Lawrence[a], B.L. Jolliff[f], B.T. Greenhagen[g], T.A. Giguere[d], D.A. Paige[h]

[a] School of Earth and Space Exploration, Arizona State University, Tempe, AZ 85281, USA
[b] Jet Propulsion Laboratory, California Institute of Technology, Pasadena, CA 91109, USA
[c] Department of Geosciences, Stony Brook University, Stony Brook, NY 11794, USA
[d] Hawaii Institute of Geophysics and Planetology, School of Ocean and Earth Science and Technology, University of Hawaii, Honolulu, HI 96822, USA
[e] Institut für Planetologie, Westfälische Wilhelms-Universität, Münster, Germany
[f] Department of Earth and Planetary Sciences, Washington University, St. Louis, MO 63105, USA
[g] Johns Hopkins University – Applied Physics Laboratory, 11100 Johns Hopkins Road, Laurel, MD 20723, USA
[h] Department of Earth and Space Sciences, University of California Los Angeles, Los Angeles, CA 90095, USA

ARTICLE INFO

Article history:
Received 24 June 2014
Revised 20 November 2015
Accepted 14 December 2015
Available online 30 December 2015

Keywords:
Moon, surface
Moon, interior
Volcanism
Infrared observations
Image processing

ABSTRACT

Lunar surface volcanic processes are dominated by mare-producing basaltic extrusions. However, spectral anomalies, landform morphology, and granitic or rhyolitic components found in the Apollo sample suites indicate limited occurrences of non-mare, geochemically evolved (Si-enriched) volcanic deposits. Recent thermal infrared spectroscopy, high-resolution imagery, and topographic data from the Lunar Reconnaissance Orbiter (LRO) show that most of the historic "red spots" and other, less well-known locations on the Moon, are indeed silica rich (relative to basalt). Here we present a geologic investigation of the Lassell massif (14.65°S, 350.96°E) near the center of Alphonsus A basin in Mare Nubium, where high-silica thermal emission signals correspond with morphological indications of viscous (possibly also explosive) extrusion, and small-scale, low-reflectance deposits occur in a variety of stratigraphic relationships. Multiple layers with stair-step lobate forms suggest different eruption events or pulsing within a single eruption. Absolute model ages derived from crater size-frequency distributions (CSFDs) indicate that the northern parts of the massif were emplaced at ~4 Ga, before the surrounding mare. However, CSFDs also indicate the possibility of more recent resurfacing events. The complex resurfacing history might be explained by either continuous resurfacing due to mass wasting and/or the emplacement of pyroclastics. Relatively low-reflectance deposits are visible at meter-scale resolutions (below detection limits for compositional analysis) at multiple locations across the massif, suggestive of pyroclastic activity, a quenched flow surface, or late-stage mafic materials. Compositional evidence from 7-band UV/VIS spectral data at the kilometer-scale and morphologic evidence for possible caldera collapse and/or explosive venting support the interpretation of a complex volcanic history for the Lassell massif.

1. Introduction

Understanding the spatial and temporal distribution of lunar volcanic deposits, their compositional range, and mechanisms of emplacement, is critical for constraining theories of lunar origin and differentiation, and for parameterizing thermal, geochemical, and crustal evolution models. Silica-rich rocks are atypical of lunar surface deposits, though physical models support the eruption of viscous lavas on the Moon if sufficient volatile pressures are present (Wilson and Head, 2003). Magmas enriched in incompatible elements (e.g., Th) typically require multiple processing episodes to form, but the observed distribution and compositional range of lunar silicic materials are difficult to explain with current models of lunar magma fractionation (e.g., Hawke et al., 2003; Hagerty et al., 2006; Jolliff et al., 2011, 2012; Kusuma et al., 2012). Nevertheless, both telescopic and orbital observations of morphologically and compositionally distinct constructs, including the nearside lunar red spots (regions of strong ultraviolet (UV) absorption), have supported non-mare, Si-rich volcanic interpretations (e.g., Whitaker, 1972a; Malin, 1974; Wood and Head, 1975; Head and McCord, 1978; Müller et al., 1986; Chevrel et al., 1999; Hawke et al., 2001, 2003; Hagerty et al., 2006; Glotch et al., 2010; Wagner et al., 2010; Glotch et al., 2011; Jolliff et al., 2011; Kusuma et al., 2012; Lawrence et al., 2014; Wilson et al., 2015).

* Corresponding author at: Jet Propulsion Laboratory, California Institute of Technology, Mail Stop 183-301, 4800 Oak Grove Dr., Pasadena, CA 91109, USA.
E-mail address: james.w.ashley@jpl.nasa.gov (J.W. Ashley).

http://dx.doi.org/10.1016/j.icarus.2015.12.036
0019-1035/

The lunar red spots (first identified based on a spectral contrast between the UV and visible) include Hansteen Alpha, Herigonius ε and π, the Gruithuisen domes, Montes Riphaeus, portions of Aristarchus crater and its plateau, and the Lassell massif (Whitaker, 1972b; Malin, 1974; Wood and Head, 1975; Bruno et al., 1991; Hawke et al., 2001). Many red spots, including the Lassell massif, correlate with anomalously high Th signatures in Lunar Prospector Gamma-Ray Spectrometer (LP GRS) data, consistent with evolved magma sources (Hawke et al., 2001; Lawrence et al., 2003; Hagerty et al., 2006). More recently, the LRO Diviner Lunar Radiometer Experiment (Diviner) directly measured thermal emission signatures considered diagnostic of highly silicic rocks in several red spot areas (Glotch et al., 2010; Greenhagen et al., 2010), within the Mairan domes (Glotch et al., 2011), and from the Compton–Belkovich Volcanic Complex (Jolliff et al., 2011).

The focus of this study is the red spot associated with the Lassell massif, which is located in Mare Nubium (Figs. 1 and 2). The Lassell region consists of Lassell crater, eleven craters over 2 km diameter, and a ~25 × 46 km, north–south oriented mountain range (the massif) (Fig. 1b). The northern portion of the massif exhibits uneven topography, previously described as mantled (Wood and Head, 1975), and the southern portion of the massif includes two large, irregularly shaped, steep-walled negative-relief features (Lassell G ~ 5 × 7 km, and Lassell K ~ 4.5 × 7 km) (Fig. 1). Here we use Diviner thermal emission spectra co-registered with Lunar Reconnaissance Orbiter Camera (LROC; Robinson et al., 2010) images and digital terrain models (DTMs) to further tie composition to regional geomorphology. We also investigate the timing of volcanic activity associated with the Lassell massif relative to the surrounding Mare Nubium deposits dated to be ~3.38 Ga old (Hiesinger et al., 2003). Interpretations of all data sets and of model ages are consistent with a silicic volcanic origin for the massif that might have been resurfaced relatively recently (either by mass wasting or pyroclastic eruptions).

2. Data products

We used LROC (Robinson et al., 2010) Wide Angle Camera (WAC; 100 m/px) images, WAC three-band (680, 415, and 321 nm; ~475 m/px) color images, the WAC Global Lunar DTM 100 m topographic model (GLD100; Scholten et al., 2012) (horizontal resolution ≃300 m/px, vertical resolution = 10–20 m), and Narrow Angle Camera (NAC; 0.5–0.9 m/px) image mosaics. Relevant mosaics were co-registered with Diviner mid-infrared emissivity spectra using the 7.8, 8.25, 8.55 μm channels at a resolution of 256 px/deg. LROC images were calibrated, map-projected, and mosaicked using United States Geological Survey (USGS) Integrated Software for Imagers and Spectrometers (ISIS) (Anderson et al., 2004). A high-resolution (2 m/px) DTM was derived from NAC stereo observations for the study area using the techniques of Tran et al. (2010) and Burns et al. (2012). A geologic sketch map was prepared from the NAC frames and DTM based on morphology, texture, and albedo, following the planetary mapping guidelines of Greeley and Batson (1990) and Tanaka et al. (2010).

Diviner three-point thermal emission spectra were used to assess surface composition. Wavelength positions of mid-infrared emissivity maxima (known as the Christiansen feature, or CF) are correlated with silica content in emissivity spectra (e.g., Logan et al., 1973). The CF occurs on the short wavelength side of prominent absorption bands at frequencies where particle size-related scattering effects are minimal, which makes it very useful for assessing the compositions of powdered materials such as the lunar regolith (e.g., Salisbury et al., 1995). Diviner emissivity near 8 μm is used to model the silicate mineral CF position (e.g., for anorthite, augite, etc.). The presence of highly silicic materials (e.g., >50 vol% SiO_2) like alkali feldspars, quartz, or silica-rich glass, which have CF positions outside of the Diviner spectral range (Glotch et al., 2010), is inferred based on the concavity of the three-point spectra near 8 μm (e.g., Glotch et al., 2010; Greenhagen et al., 2010). Additional data products used in this study include Clementine UVVIS camera iron (FeO) and titanium (TiO_2) abundance maps (e.g., Lucey et al., 2000a; Gillis et al., 2004) and the optical maturity parameter map (Lucey et al., 2000b). Clementine abundance maps are used to explore kilometer-scale geochemistry of the Lassell massif and its immediate surroundings.

3. Observations

Among the more significant features found in these data products, we observe (1) morphologies and spectral characteristics

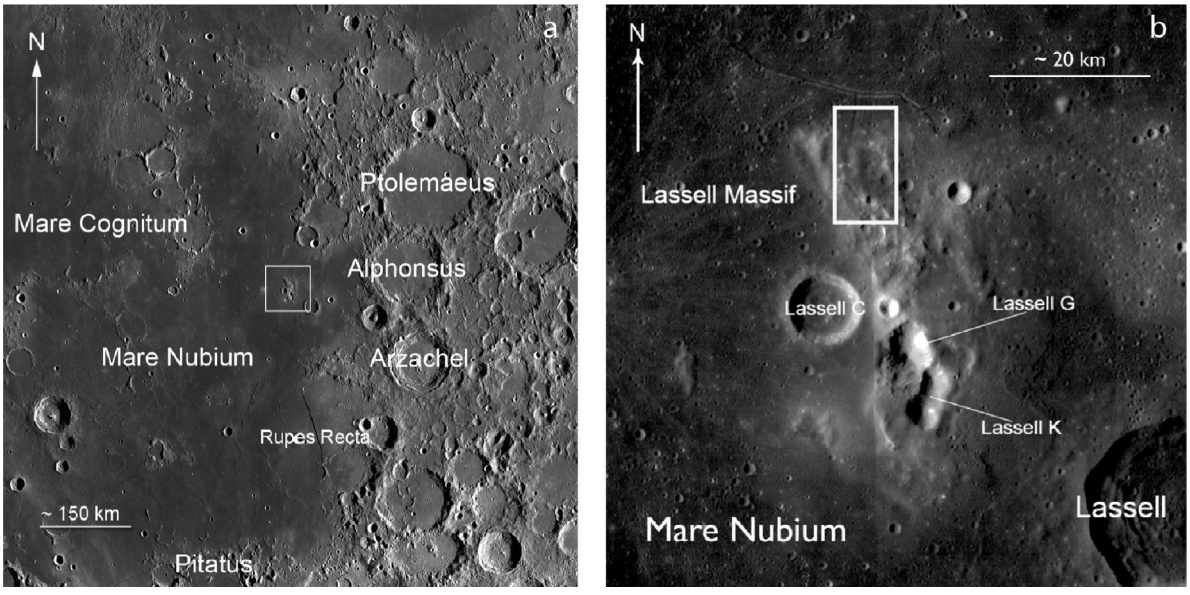

Fig. 1. (a) WAC mosaic of Lassell massif complex (white box) in regional context. (b) Lassell massif. White rectangle indicates the region where CSFD measurements were performed (see Section 3, Age estimates; and Figs. 10 and 11).

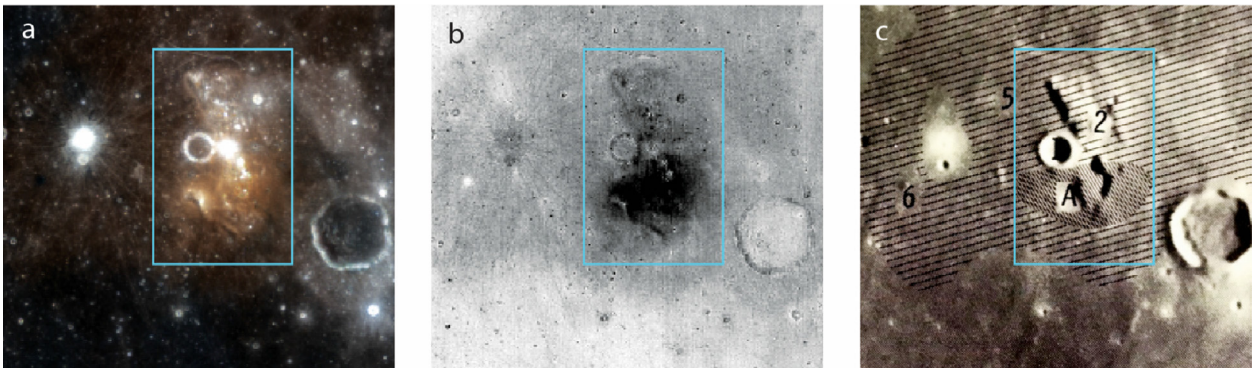

Fig. 2. (a) WAC color composite using bands centered at 689, 415, and 321 nm; where the 689, 415, and 321 bands are represented as R, G, B, respectively; image width 60 km. Note strong red anomaly (415 nm absorption) associated with the southern half of the Lassell massif. (b) WAC 321/415 nm ratio map; darker areas correspond to a lower ratio and are more UV absorbing. (c) Visually red zone observed by ground-based observatories (hatched zone A; other hatched zones are less red areas) reproduced from Whitaker (1972a). Cyan outlines are intended to assist with massif location and comparison between images. (For interpretation of the references to color in this figure legend, the reader is referred to the web version of this article.)

typically associated with volcanic processes, (2) stratigraphic relationships indicating a volcanic sequence of events, and (3) outcrops of relatively low-reflectance materials consistent with pyroclastic or intercalated flow deposits. Descriptions are summarized in the following subsections, with interpretations presented in Section 4.

3.1. Large-scale morphologic and spectral observations

The WAC three-band color composite (Fig. 2a) and a 321/415 nm ratio map (Fig. 2b) indicate that the southern half of Lassell massif is more UV-absorbing than the northern half, consistent with previous UV–VIS observations (e.g., Whitaker, 1972b; and Fig. 2c). The visually reddish coloration noted from both Earth-based telescopic observations and by astronauts in lunar orbit (Whitaker, 1972a, 1972b) is produced by preferential absorption below ~500 nm. Large-scale views of the morphology and topographic relief of the Lassell massif are provided by an oblique NAC observation (M1111904689R) (Fig. 3) and the WAC GLD100 DTM (Fig. 4). The NAC-derived DTM and geologic sketch map (Figs. 5 and 6) present the major landforms identifiable from NAC frames. The deepest pits of unit iC (Lassell G and K) are mapped together with additional negative-relief features exhibiting similarly irregular, arcuate margins to the east and southeast (e.g., black arrow in Fig. 4). Lassell G and K are separated by a steep ridge, in contrast to the northern portion of the massif, which is dominated by less-rugged but still hummocky topography (unit uM). A linear rille is located approximately 5 km north of the massif. The area north of the rille (Fig. 4, white arrow) is 25 m lower than mare surfaces south of the rille, indicating a vertical offset and possible tectonic control for the rille system.

The NAC DTM (Fig. 5; 2 m/px sampling) covers approximately ~110 km^2 of the region centered on the Lassell massif and includes the eastern half of Lassell C crater. The floor of 8.6 km-diameter Lassell C crater (Figs. 1b and 3) is hummocky (unit Hf) and does not exhibit any superposed impact craters larger than ~250 m in diameter. The DTM shows the Lassell massif rising more than 520 m above the surrounding plains with slopes averaging ~8° and ranging up to ~31° in the northern portion. The steepest slope within the deepest of the markedly funnel-shaped, negative-relief features in the southern portion of the massif (Lassell G) is approximately 55° from horizontal. The bottom of Lassell G is nearly 1160 m below the surrounding plains. Lassell G and K have maximum depth-to-diameter ratios (d/D) of 0.19 and 0.21, respectively (measured from the highest rim to lowest interior points), with values averaging at 0.14 for Lassell G and 0.16 for Lassell K due to highly irregular diameters and rim elevations. This wide d/D variation means that d/D values may not be particularly meaningful morphometric parameters for Lassell G and K, but they are offered for qualitative comparison with typical d/D ratios of fresh craters in the diameter range of Lassell G and K, which are expected to be near 0.2 (Pike, 1977; Melosh and Ivanov, 1999; Stopar et al., 2014a; Mahanti et al., 2014). However, unlike typical fresh impact craters, Lassell G and K lack any obvious upraised rims or ejecta blankets.

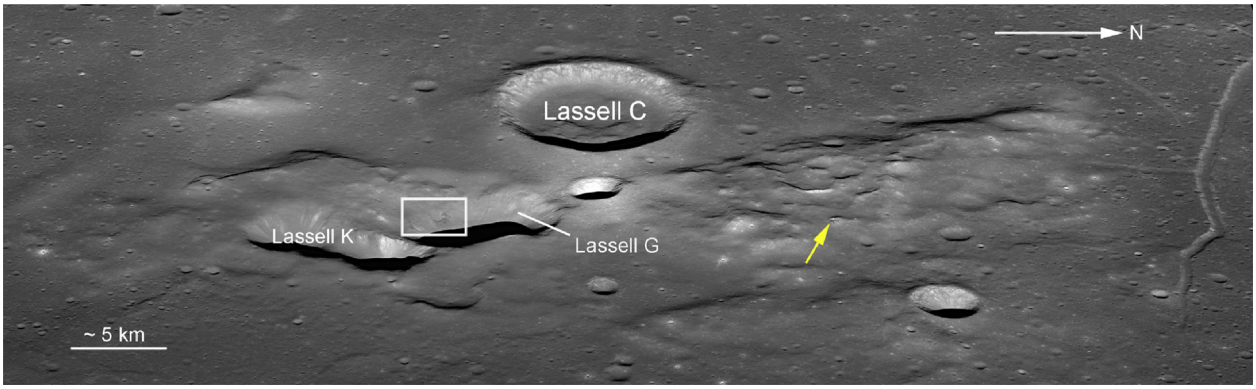

Fig. 3. NAC oblique frame (M1108311369) showing the entire massif from the east looking west; incidence angle = 72.3°, emission angle = 62.6°, pixel scale = 2.2 m, no vertical exaggeration. Yellow arrow indicates impact crater in Fig. 14b. White box is area shown in Fig. 14c. (For interpretation of the references to color in this figure legend, the reader is referred to the web version of this article.)

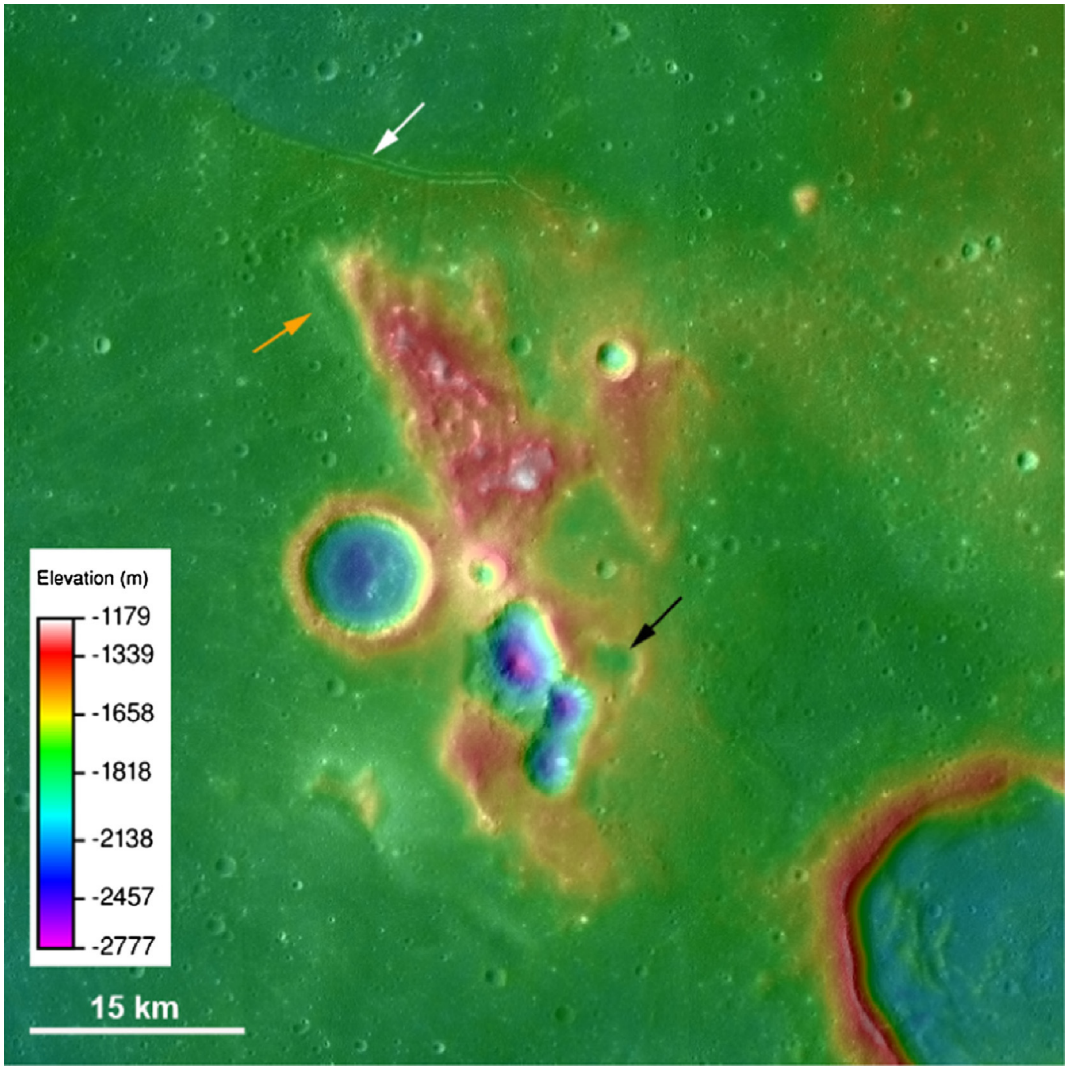

Fig. 4. WAC DTM superposed on shaded relief. White arrow indicates tectonically controlled rille (note slightly lower (bluer) elevations north of rille); orange arrow shows the margin of unit lM (see Fig. 6); black arrow indicates a relatively shallow negative-relief feature, suggested to be an infilled or partially collapsed portion of caldera complex. (For interpretation of the references to color in this figure legend, the reader is referred to the web version of this article.)

A Si-rich Diviner signature correlates with massif morphology, with the shortest wavelength CF values concentrating in the southern half of the landform (Fig. 7), coincident with much of the UV-absorbing region (Fig. 2b). The strongest Si-rich signatures in the northern portion of the massif tend to be discontinuous and of lesser spatial extent than those in the southern portion. Many are associated with hummocks and impact features, which may expose Si-rich material ordinarily buried by regolith. Strong Si-rich Diviner signals and UV absorptions are not evident within Lassell C crater.

New Clementine FeO and TiO_2 abundance maps were prepared for this research using Clementine UVVIS observations (415–1000 nm). These maps employ algorithms that rely on band ratio plots versus reflectance, calibrated to returned soil sample analysis (Lucey et al., 2000a), and show low-concentrations FeO and TiO_2 over the southern portion of the massif and terrain to the southwest (Fig. 8).

3.2. Stratigraphic relationships

Previous observations suggested an embayment relationship between Mare Nubium basalts and the Lassell edifice (e.g., Hawke and Head, 1977; Müller et al., 1986) with the interpretation that at least portions of the massif predate mare emplacement at ~3.38 Ga (Hiesinger et al., 2003). The WAC DTM (Fig. 4) shows that while many contacts surrounding the massif do indeed appear arcuate with abrupt changes in slope, which would be expected from embayment, an unambiguous time-stratigraphic relationship is not necessarily straightforward along all massif contacts with the surrounding mare deposits. A small, previously unrecognized, conical positive relief feature underlies a lobate deposit at the south end of the massif (Fig. 9; units sP and sC). Although it may simply be a degraded impact crater, this feature has interior rim slopes of ~5°, exterior flank slopes of 4–10°, and is similar in height (60 m), base diameter (1850 m), and summit diameter (740 m) to a lunar basaltic cone (e.g., Wood, 1979; Weitz and Head, 1999; Lawrence et al., 2013; Stopar et al., 2014b) (Fig. 10). A candidate cone similar in morphology is also identified at the silicic Compton–Belkovich Volcanic Complex in the northern highlands (Fig. 10b); however, neither the Lassell nor the Compton–Belkovich cone candidates exhibit the prominent blocky outcrops that are common in the Marius Hills (and other) basaltic cones (e.g., Fig. 10a). A series of lobate forms each 35–45 m in height with margin slopes ranging from 9° to 15° are prominent in the NAC DTM along the southwestern flank of the massif in a stair-step arrangement,

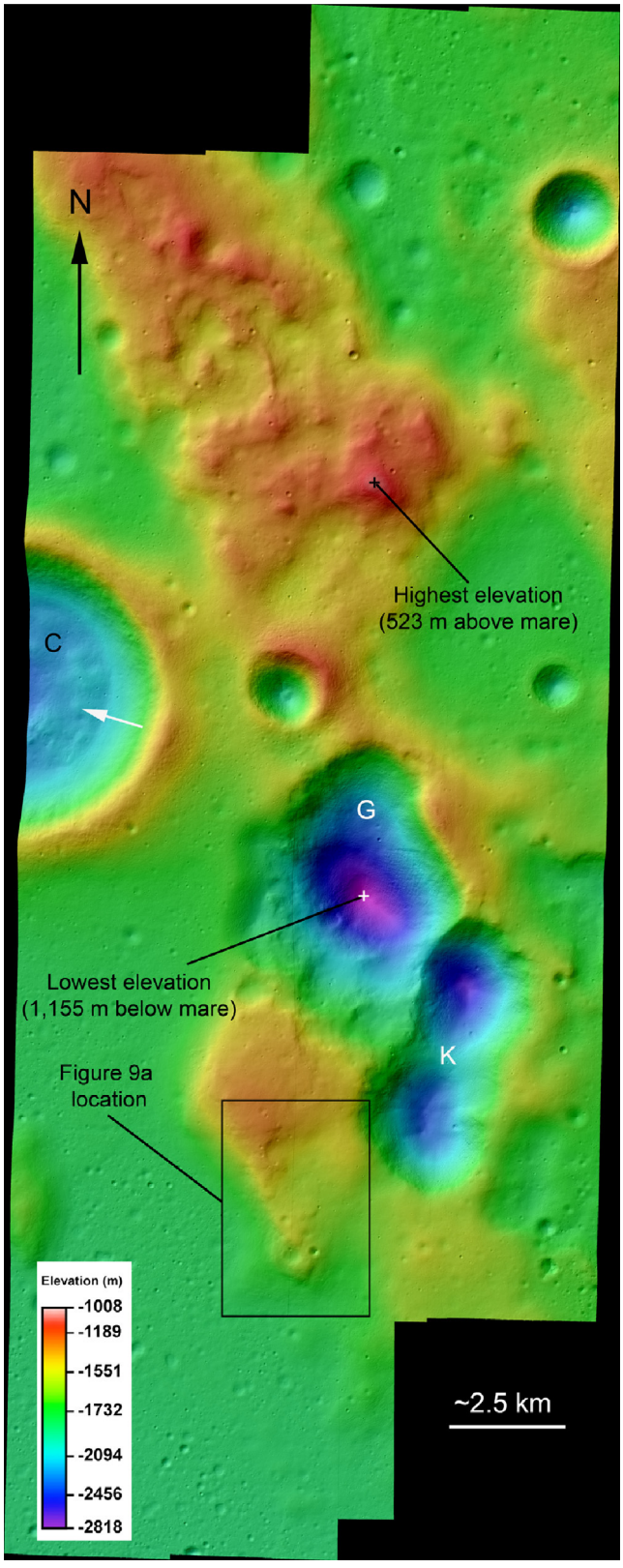

Fig. 5. NAC DTM mosaic (post spacing of 2 m) including the main portion of the massif construct. Lassell C presents asymmetric accumulations of debris that thicken toward the eastern rim (light blue hummocks and unit Hf in Fig. 6; white arrow). (For interpretation of the references to color in this figure legend, the reader is referred to the web version of this article.)

but are not evident elsewhere on the massif (Fig. 9). Lobate flows of similar heights and slopes are reported for the Marius Hills, where elevated-viscosity basaltic volcanism occurred in association with domes and cones (Lawrence et al., 2013).

The lower massif unit (lM) is interpreted as being stratigraphically lower and therefore older than the upper massif unit (uM). The candidate cone at Lassell appears superposed on the unit lM (Fig. 6), consistent with lM being an older flow. The cone landform also appears to occupy a stratigraphically intermediate position between units lM and uM. The lM unit extends beyond the upper massif into the mare to the west as a group of discontinuous mounds (visible in Fig. 4). Portions of unit lM are also UV-absorbing (Fig. 2b), such as the deposit extending westward beyond the northern massif perimeter (e.g., orange arrow in Fig. 4, and visible at the northwest end of Fig. 6). While portions of material mapped as unit lM may be older volcanic flow deposits, other portions may simply represent a debris apron mass-wasted from the massif. As there is no obvious way to distinguish between these two sources with the available data, the feature is currently mapped as a single, "lower massif" unit, representing a possible mixture of both volcanic and debris flow deposits.

3.3. Age estimates

Crater size-frequency distribution (CSFD) measurements were performed on a portion of the northern hummocky massif terrain (uM and lM) using established techniques for the definition of the count areas and measurements, as well as for the exclusion of secondary craters (e.g., Hartmann, 1966; Crater Analysis Techniques Working Group, 1979; Neukum, 1983; Hiesinger et al., 2000). We used CraterTools within ArcGIS (Kneissl et al., 2011) to make the measurements. The CSFDs were plotted and fit with CraterStats2 (Michael and Neukum, 2010), using the production function and lunar chronology of Neukum et al. (2001), valid for craters >0.01 and <100 km in diameter. The error bars represent statistical errors based on the numbers of craters counted, rather than systemic errors in the calibration of the chronology function and/or uncertainties in the production function (e.g., Michael and Neukum, 2010).

We counted 869 craters in a ~30.6 km^2 area, which we separated into two geomorphologic units—a 21.6 km^2 peripheral unit designated uMp, and a 9 km^2 central unit with small-scale hummocky texture, designated uMc (Fig. 11a). The boundary for the uMp area was drawn to encompass the flattest region in the uM unit in the northern part of the massif. We did not include the larger craters directly south of the count area because (1) they exhibit steep slopes, which result in rapid erosion and removal of small craters, and (2) their impact origin could not be unequivocally established as some of the excluded craters may be volcanic in origin. Unit uMc was mapped separately from uMp because uMc is slightly rougher, appears brighter than the adjacent terrain, and lies at a higher elevation than unit uMp. In addition, uMc exhibits a much lower crater density than uMp, suggesting a younger surface age (Fig. 11b). The oldest of the derived absolute model ages (uMp: 4.07 + 0.05/−0.08 Ga; $N(1) = 9.68 \times 10^{-2}$) likely represents the emplacement of this portion of the Lassell complex (Fig. 12). A CSFD measurement of the northern Lassell massif (274^2 km; Fig. 11c) based on lower resolution WAC imagery revealed a similar age of 3.95 Ga (+0.06/−0.09 Ga) ($N(1) = 4.68 \times 10^{-2}$) (Fig. 12). Thus, both WAC- and NAC-based CSFD measurements of large craters (>1 km) are roughly consistent with each other, despite different spatial resolutions, illumination conditions (Soderblom, 1970;

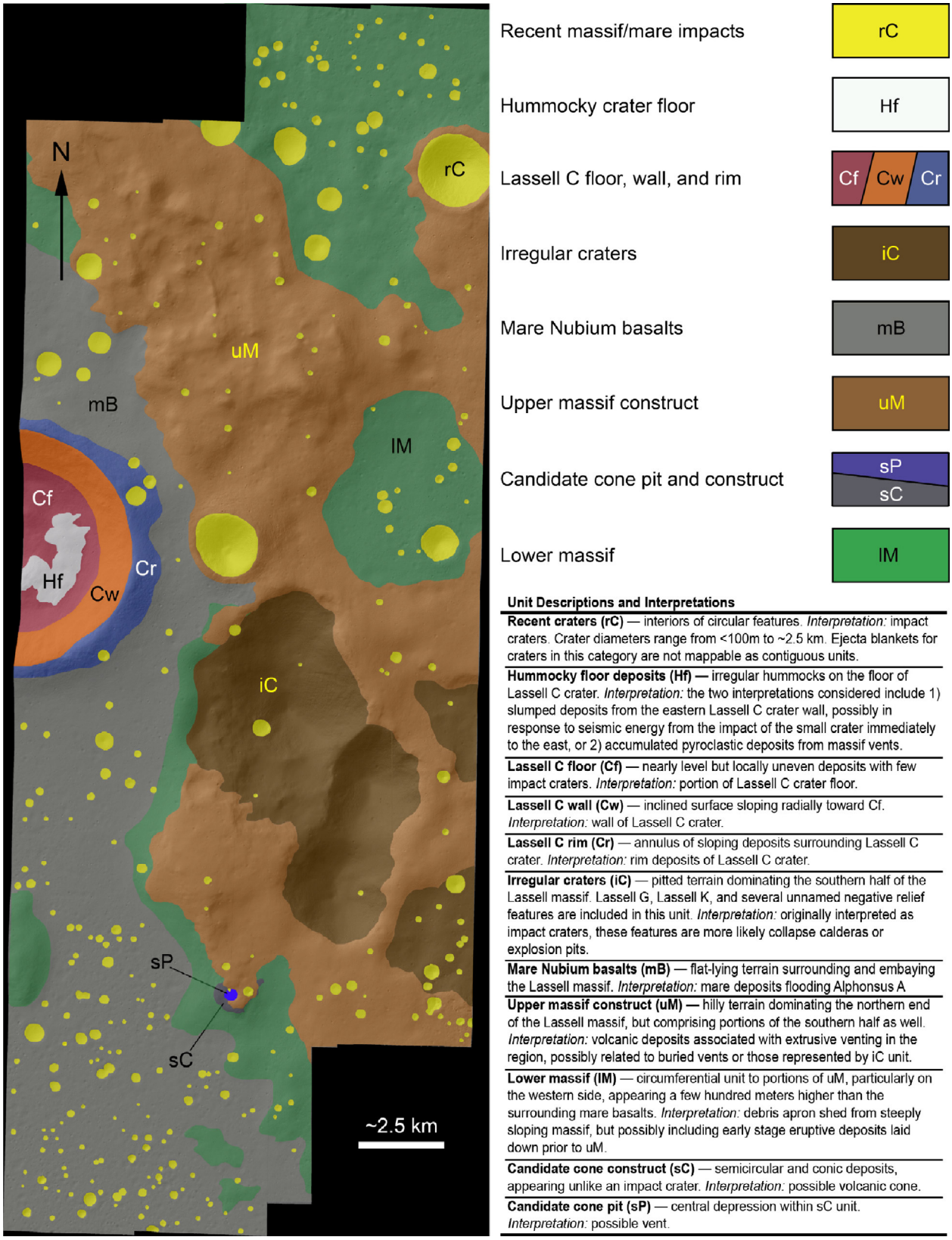

Unit Descriptions and Interpretations

Recent craters (rC) — interiors of circular features. *Interpretation:* impact craters. Crater diameters range from <100m to ~2.5 km. Ejecta blankets for craters in this category are not mappable as contiguous units.

Hummocky floor deposits (Hf) — irregular hummocks on the floor of Lassell C crater. *Interpretation:* the two interpretations considered include 1) slumped deposits from the eastern Lassell C crater wall, possibly in response to seismic energy from the impact of the small crater immediately to the east, or 2) accumulated pyroclastic deposits from massif vents.

Lassell C floor (Cf) — nearly level but locally uneven deposits with few impact craters. *Interpretation:* portion of Lassell C crater floor.

Lassell C wall (Cw) — inclined surface sloping radially toward Cf. *Interpretation:* wall of Lassell C crater.

Lassell C rim (Cr) — annulus of sloping deposits surrounding Lassell C crater. *Interpretation:* rim deposits of Lassell C crater.

Irregular craters (iC) — pitted terrain dominating the southern half of the Lassell massif. Lassell G, Lassell K, and several unnamed negative relief features are included in this unit. *Interpretation:* originally interpreted as impact craters, these features are more likely collapse calderas or explosion pits.

Mare Nubium basalts (mB) — flat-lying terrain surrounding and embaying the Lassell massif. *Interpretation:* mare deposits flooding Alphonsus A

Upper massif construct (uM) — hilly terrain dominating the northern end of the Lassell massif, but comprising portions of the southern half as well. *Interpretation:* volcanic deposits associated with extrusive venting in the region, possibly related to buried vents or those represented by iC unit.

Lower massif (lM) — circumferential unit to portions of uM, particularly on the western side, appearing a few hundred meters higher than the surrounding mare basalts. *Interpretation:* debris apron shed from steeply sloping massif, but possibly including early stage eruptive deposits laid down prior to uM.

Candidate cone construct (sC) — semicircular and conic deposits, appearing unlike an impact crater. *Interpretation:* possible volcanic cone.

Candidate cone pit (sP) — central depression within sC unit. *Interpretation:* possible vent.

Fig. 6. Geologic sketch map, unit key, unit descriptions, and interpretations based on morphology within the WAC and NAC DTMs, and NAC frames.

Young, 1975; Wilcox et al., 2005; Ostrach et al., 2011), and sizes of the count areas (Pasckert et al., 2015; van der Bogert et al., 2015). In unit uMp, craters with diameters of ~130–150 m may record a discrete resurfacing event at about 900 Ma, while craters with diameters of ~80–100 m may show a resurfacing event at about 400 Ma. These events could represent minor shaking caused by the formation of nearby Copernican craters. Such discrete resurfacing events could not, however, be unambiguously identified because

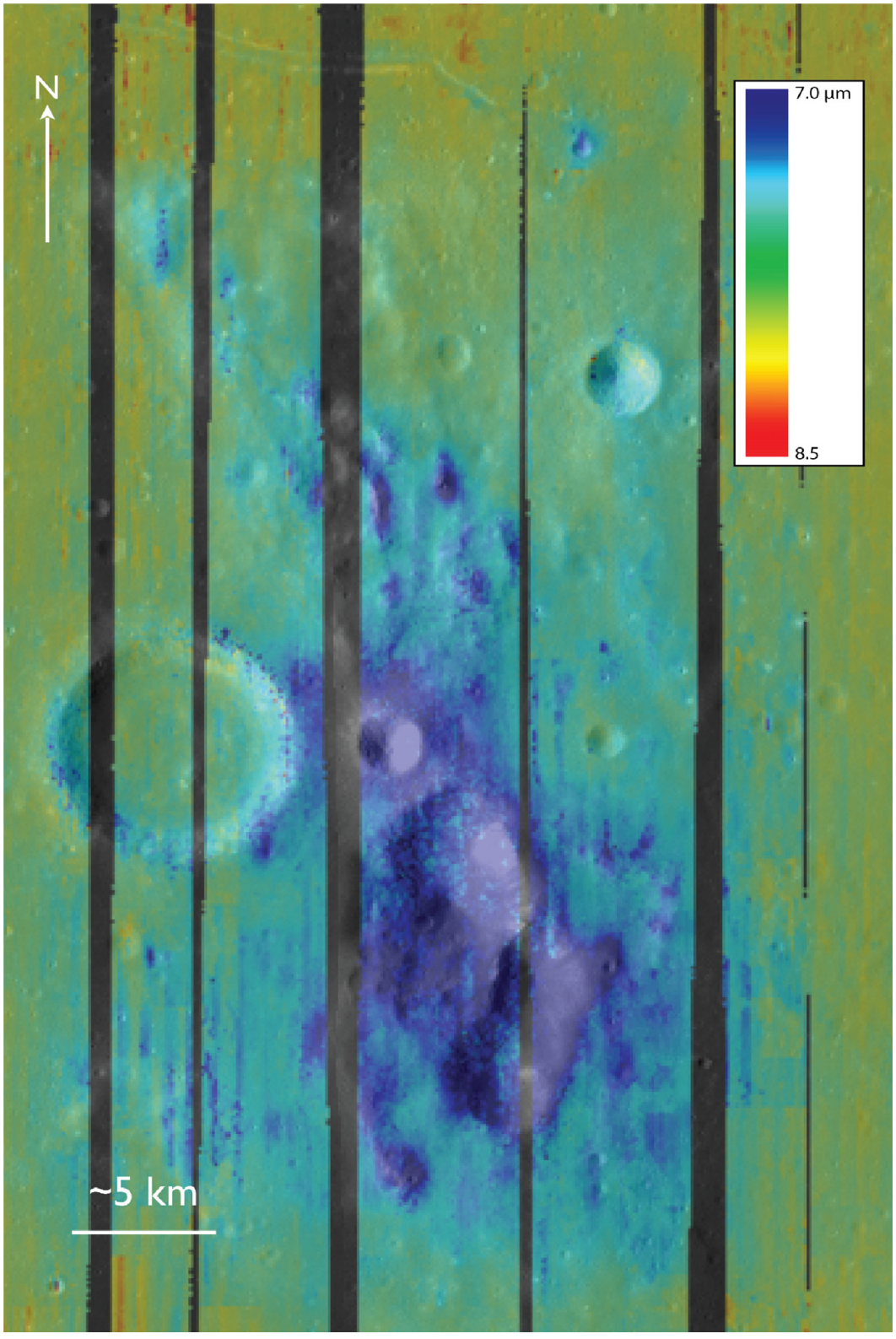

Fig. 7. Diviner map of the Christiansen feature (CF), binned at 256 px/deg, and co-registered with LROC WAC GLD100 shaded relief map. Color scale ranges from CF values of 7 μm (silica-rich; blue) to 8.5 μm (silica-poor; red). (For interpretation of the references to color in this figure legend, the reader is referred to the web version of this article.)

the CSFD never steepens enough to clearly follow the production function over a significant crater diameter range. The CSFD for craters <80 m in diameter in unit uMp show continuous resurfacing, indicative of a quasi-equilibrium condition (parallel to the nominal lunar equilibrium curve). Thus additional absolute model ages could not be fit. The central uMc area has an absolute model age of 58 ± 4.1 Ma with an $N(1)$ of 4.86×10^{-5}. This age most likely represents the age of the local regolith, but could also be

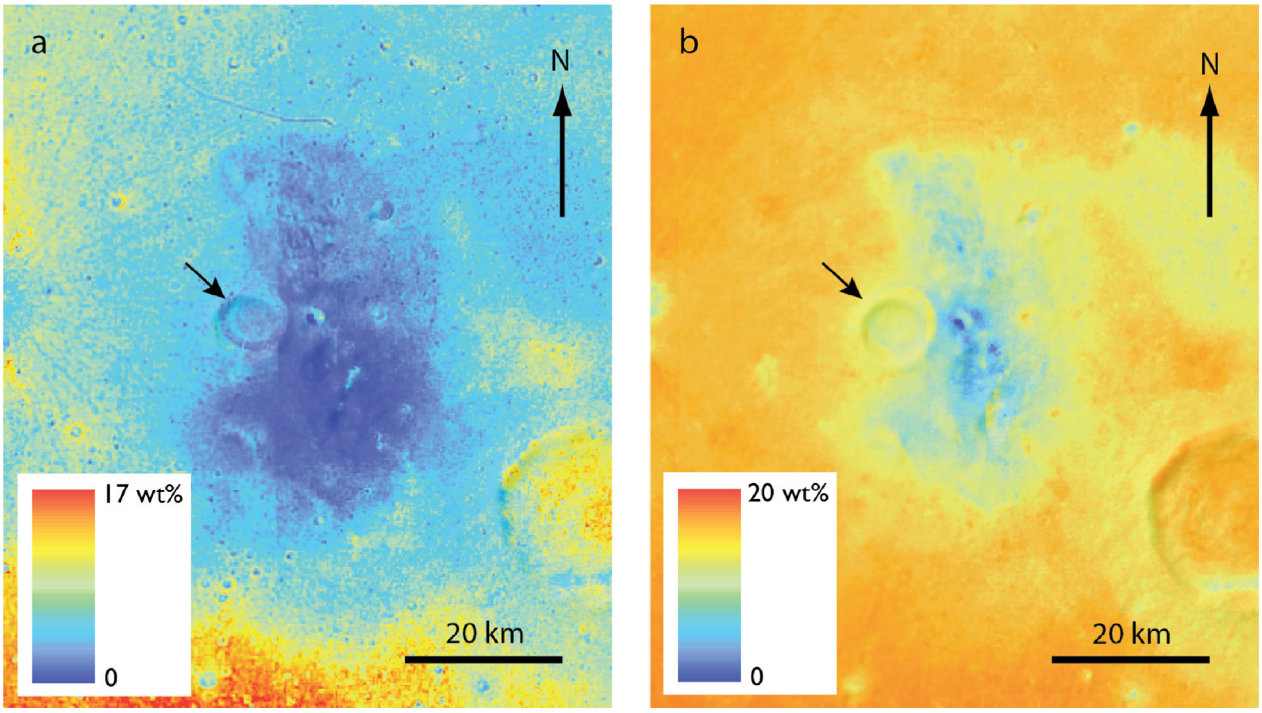

Fig. 8. Relatively low-concentrations FeO (a) and TiO_2 (b) are associated with the massif; values in weight percent derived using the methods of Lucey et al. (2000a). Arrows indicate Lassell C.

caused by a difference in crater scaling between the strength- and gravity-controlled regimes for this target material (van der Bogert et al., this issue). The uMc CSFD also shows hints for discrete resurfacing at around 400 Ma, but this age is not well supported by the CSFDs and remains highly speculative.

Generally, the massif is very difficult to date with CSFD measurements because of various effects, including the limited size of the study area, steep slopes, resurfacing, subdued crater morphologies, possible effects of target properties (Schultz et al., 1977; Dundas et al., 2010; van der Bogert et al., this issue), and the complex geologic history. In particular, in some cases it is difficult to distinguish between volcanic vents and degraded impact craters. In summary, for the reasons stated above, the CSFD measurements can only provide general information about the ages of the units.

3.4. Low-reflectance deposits

Relatively low-reflectance linear streamers and patches up to ~350 m across in the walls of Lassell G and K exhibit the highest contrast in low-incidence angle (Sun angle measured from the surface normal) NAC frames (Figs. 13 and 14). The Mare Nubium deposits surrounding the massif are low-reflectance (mature) materials suitable for albedo comparison with the patches on the massif, which appear dark in stretched images. These mare deposits present I/F values of 0.05 in the same image where the low-reflectance patches present I/F values of 0.055. For comparison, the higher reflectance, immature materials on the massif have I/F values around 0.126. The I/F of the streamers inside Lassell craters G and K have values comparable to those for nearby mare basalts despite the fact the dark streamers have lower phase angles (steep slope with azimuth toward Sun) than the horizontal mare materials. Some of these deposits are block-rich, with block diameters up to ~4.5 m. Block occurrences within these deposits are greatest upslope. Localized low-reflectance deposits are also seen in the northern half of the massif, excavated and exposed through impact cratering (Fig. 14b and yellow arrow in Fig. 3).

4. Discussion

4.1. Evidence for Si-rich volcanism

There are several lines of evidence supporting a Si-rich origin for the Lassell massif. The Diviner CF map identifies a region of high-Si materials centered on Lassell G and K that extends to the northern massif region and the southwest (Fig. 7). Some outlying detections of silicic materials are coincident with small impact craters and steep slopes. These may result from excavated deposits slope-effects, and/or rocky surfaces. Steep slopes can lead to sub-pixel anisothermality in the Diviner emission data, which, depending on exact conditions could shift the apparent CF position of the surface to shorter wavelengths, resulting in a false detection of Si-rich surfaces (Greenhagen et al., 2010). In this work, we employed the empirical correction of Greenhagen et al. (2010) to compensate for the effects of sub-pixel temperature variations in the Diviner data set, resulting in emissivity values that are normalized to zero degrees solar incidence angle at the lunar equator. This minimization of the anisothermality effect provides confidence to the interpretation of these small-area, short-wavelength CF values as real concentrations of Si-rich materials.

Based on Diviner data, the northeastern portion of the candidate cone in Fig. 10c appears to be more silicic than the southwestern portion (Fig. 9c). Such a relationship could imply a compositionally diverse sequence of extrusive events. Alternatively, mixing, degradation, or partial collapse of the feature may simply have obscured the original composition of the older, lower units (lM). We interpret the stair-step, lobate forms visible above the candidate cone and along the southern portion of the massif (black arrows in Fig. 9a and b) to be consistent with multiple, viscous extrusion events (originating from an unknown source vent, or possibly

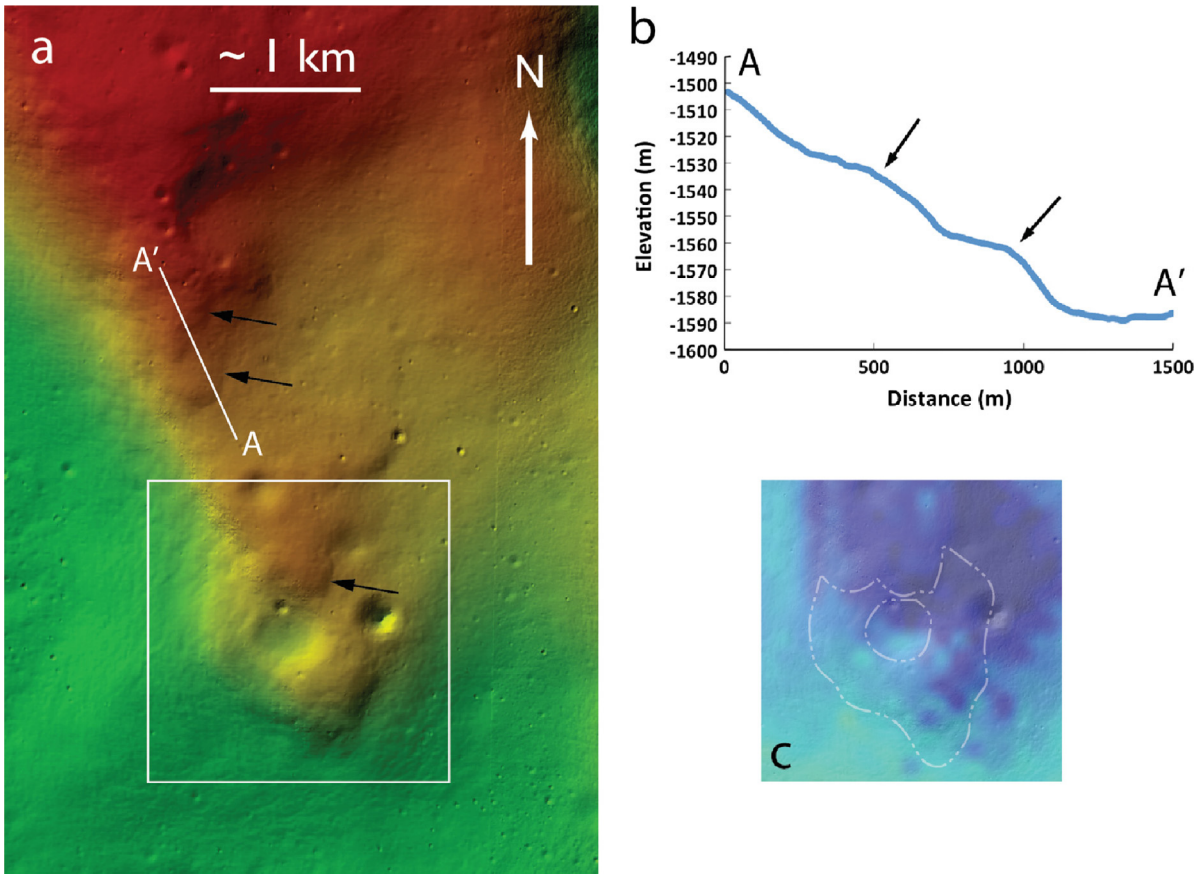

Fig. 9. (a) Detail of NAC DTM with color scale stretched to highlight the morphology of the candidate cone (green is lower elevation, red is higher elevation), showing southern margin of Lassell massif (see Figs. 5 and 6 for context). Arrows indicate margins of lobate flow structures in stair-step arrangement. The lobes superpose the candidate volcanic cone structure; also presented at NAC resolution as Fig. 10c. (b) Topographic profile A–A′ traverses two of the lobate forms highlighted in (a) (arrows reproduced for clarity). Breaks in slope are easily identified. (c) Diviner CF map of candidate cone representing white box area in (a), registered to cylindrically projected NAC shaded relief base image. Dark blue indicates relatively high silica; dashed outline indicates candidate cone margins. Note that CF values representing different silica compositions correspond roughly to morphologically distinct deposits representing the northeast and southwest halves of the structure. (For interpretation of the references to color in this figure legend, the reader is referred to the web version of this article.)

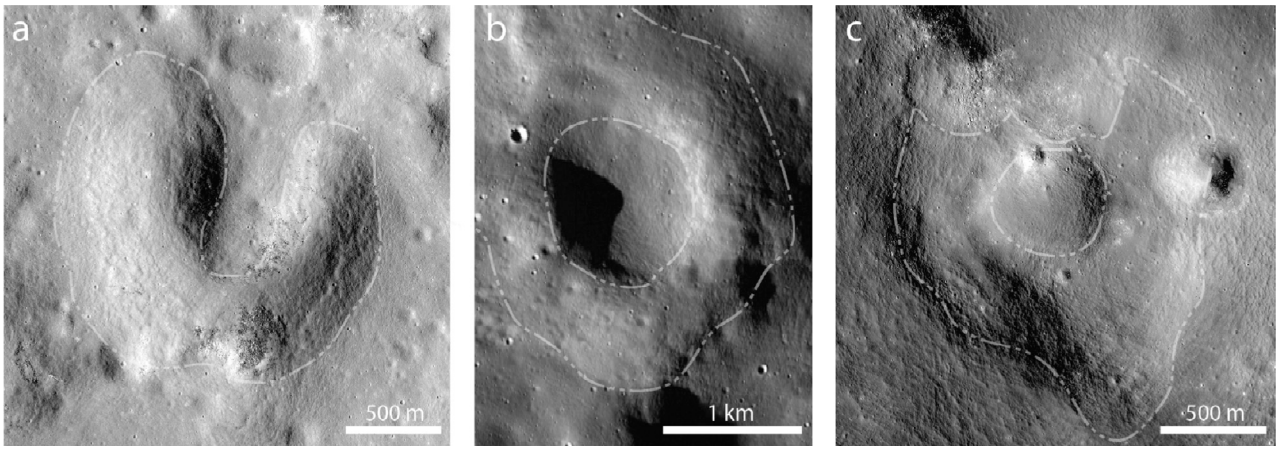

Fig. 10. (a) Basaltic C-shaped volcanic cone in the Marius Hills (NAC M150877632R). Note the blocky layers as outcrops. (b) Candidate volcanic cone within the Compton–Belkovich Volcanic Complex (NAC M119219248L). Compare with the Lassell feature: (c) NAC image of candidate volcanic cone (M160010100R). This conical feature is 60 m in height and 1850 m in diameter at its base, and has a 740 m diameter summit crater. Semitransparent, dashed outlines are provided to assist with identification of features.

Lassell G), with at least one lobe of silicic composition that overlies the northwest portion of the cone. The strong correlation of these lobes with the Diviner Si-rich signatures (Fig. 7), combined with modeled Th enhancement (Hagerty et al., 2006), makes a compelling case for non-mare (silicic) volcanism from geochemically evolved magma sources.

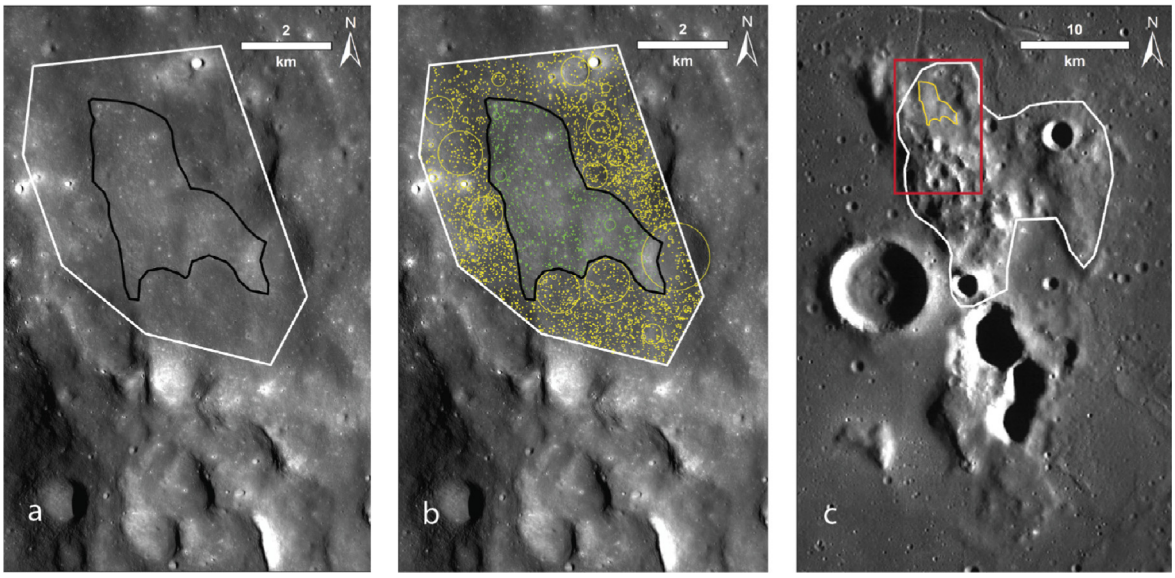

Fig. 11. Count areas for the crater size-frequency distributions (CSFDs). (a) Two different geomorphologic units were identified and measured at NAC resolution. The area between the black and white boundaries is the 21.6 km^2 uMp (peripheral) unit; within the black line is the 9 km^2 uMc (central) unit. (b) Locations of craters in the uMp (yellow) and uMc (green) count areas. The peripheral unit is more heavily cratered than the central unit. (c) An area encompassing both uM and lM units was also measured at WAC resolution (white outline). Red outline shows (a and b) area; yellow outline shows uMc unit location. (For interpretation of the references to color in this figure legend, the reader is referred to the web version of this article.)

Evidence that Lassell G and K are unlikely to be impact craters is found in an absence of associated raised rims or ejecta blankets (which even a low-velocity secondary bolide should produce at the scale of the NAC DTM) together with their steep interior walls. Their arcuate margins are similar to those found in many terrestrial and planetary volcanic caldera settings where magma contraction or withdrawal leads to surface collapse, as proposed for the Mairan domes (Glotch et al., 2011) and the Compton–Belkovich Volcanic Complex (Jolliff et al., 2011). Lassell G and K and the rest of the iC unit are likely part of such a collapse caldera, explosion pits, or a combination of both. The steep (>25°) and fresh-appearing interior slopes of the craters Lassell G and K further suggest relatively recent eruptive activity or, alternatively, ongoing mass wasting of these features. Forward-modeling of the Lunar Prospector (LP) Th concentrations suggest that the LP signature cannot be reproduced unless both the northern massif and Lassell G and K have elevated Th concentrations (Hagerty et al., 2006); the modeling results indicate Th concentrations of 53 ± 5 ppm for the northern massif and 25 ± 2 ppm for the Lassell G and K area. The modeled elevated Th concentrations further suggest that Lassell G and K are compositionally related to the northern massif, consistent with volcanic deposition from a central vent or caldera (now buried). For comparison, Th concentration values for other non-mare volcanic landforms on the Moon include 10 ppm for the Compton–Belkovich Volcanic Complex (e.g., Jolliff et al., 2011), and 19.5 ± 1.6 ppm, 43 ± 3 ppm, and 17 ± 6 ppm for Hansteen Alpha, Gruithuisen γ, and Gruithuisen δ, respectively (Hagerty et al., 2006).

4.2. Timing of emplacement

The interpretation of a pre-mare emplacement for the Lassell massif based on apparent embayment by surrounding mare deposits (e.g., Müller et al., 1986) is supported by absolute model ages derived from CSFDs (Fig. 12), which indicate that the northern parts of the massif (uMp) were indeed emplaced at ~4 Ga, before the surrounding mare (~3.38 Ga; Hiesinger et al., 2003). However the steepness and freshness of Lassell G and K walls, stratigraphic relationships, and CSFDs suggests the possibility for additional, post-mare resurfacing. Craters in unit uMp with diameters >80 m indicate possible discrete resurfacing events at about 900 and 400 Ma, potentially associated with shaking caused by the formation of nearby Copernican craters, while craters <80 m in diameter exhibit characteristics of continuous resurfacing. Continuous crater degradation through mass wasting and/or pyroclastic mantling are possible explanations. The central part of the northern Lassell massif (unit uMc) may have been resurfaced as recently as 60 Ma, although this age could simply represent that of the local regolith. If the resurfacing resulted from pyroclastic mantling, such anomalously recent volcanic activity demands further exploration, and significant modifications to existing thermal models for the Moon are required to account for such (isolated) volcanic activity occurring so recently. Additional, independent evidence for basaltic volcanism occurring on the Moon within the last 100 Ma supports this possibility (Braden et al., 2014). However, the CSFD measurements are affected by different factors that might influence the derived ages and their interpretation. Those factors are the complex geology of the area, the limited spatial extent of the units to be dated, the topography, the extreme degradation of some craters, and, at least in a few cases, the difficulty to unambiguously distinguish impact craters from volcanic vents. In addition, craters smaller than ~400 m in diameter form in the strength-scaling regime, rather than in the gravity-scaling regime, such that the properties of the surface can cause discrepancies in the final crater diameters and, as a result, the derived absolute model ages (van der Bogert et al., this issue).

4.3. Low-reflectance deposits

Small exposures of relatively low-reflectance deposits along the margins of Lassell G and K, and elsewhere throughout the lM and uM units (Fig. 14), suggest that a thin layer of low-reflectance material may lie just beneath the regolith over portions of the massif. This material is exposed through mass wasting along the steep

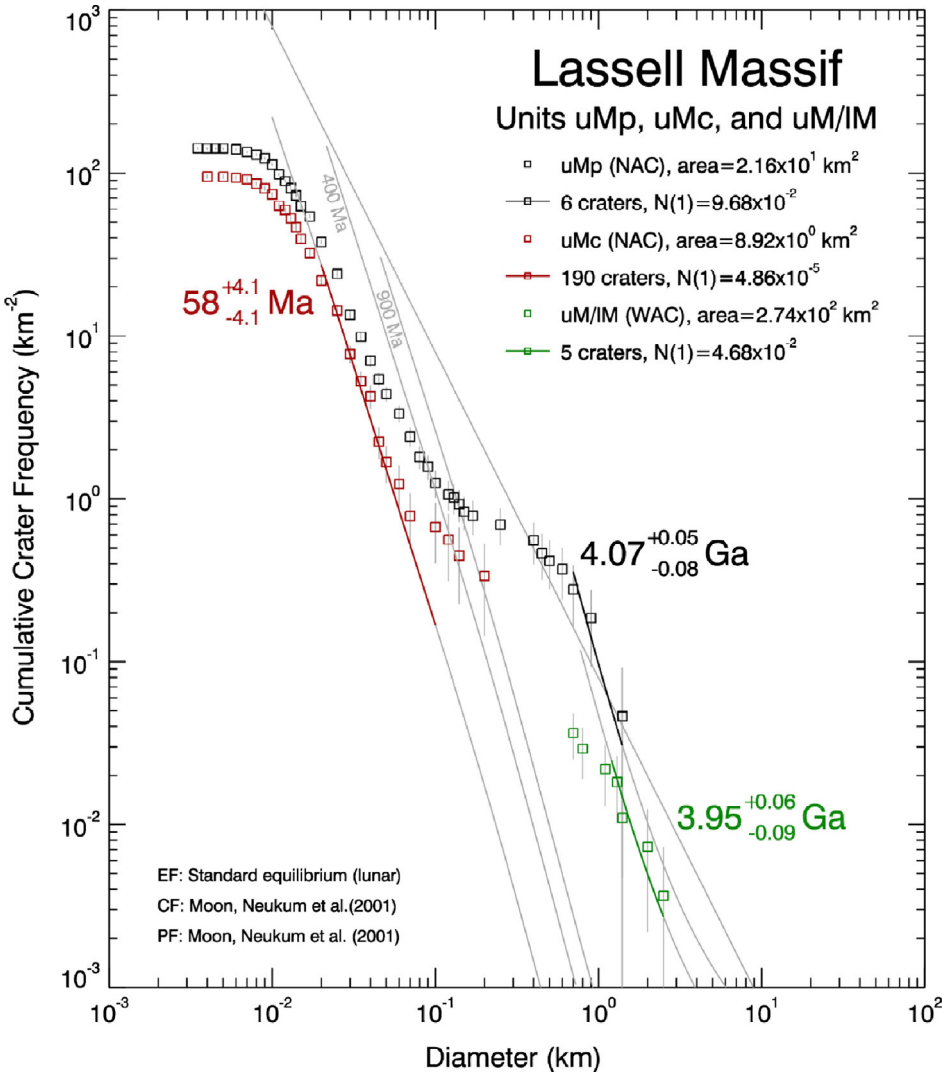

Fig. 12. CSFD measurements for the uMp unit (black) uMc unit (red), and the northern Lassell massif (green). The CSFD for the uMp area is complex, suggesting multiple resurfacing events, with a ~4 Ga age for the core of Lassell massif itself. The uMc area may have been resurfaced within the past 60 Ma, with this age most likely representing that of the local regolith. Other discrete resurfacing events may have occurred at 900 and 400 Ma, perhaps in connection with shaking caused by nearby Copernican crater formation. However, the absence of obvious discrete events would suggest long-term mass-wasting or surface property effects. (For interpretation of the references to color in this figure legend, the reader is referred to the web version of this article.)

slopes of Lassell G and K, and has been excavated by impact elsewhere on the massif (Fig. 3, at tip of yellow arrow; Fig. 14b). The low-reflectance deposits may represent late-stage basaltic eruptions, pyroclastic materials, volatile-depleted or quenched surface crust materials, or mare contamination. The sometimes-blocky appearance of these deposits suggests at least a partly coherent material, but its composition remains unknown because its spatial extent (meter-scale) falls well below the detection capability of current instrumentation (kilometer-scale). The association of these low-reflectance deposits with some of the highest silica and lowest FeO concentrations in the study area is consistent with a silicic composition (i.e., a quenched flow surface). However, similar exposures of low-reflectance deposits are observed in regional dark mantle deposits (RDMDs) including Sulpicius Gallus, Taurus-Littrow, and Aristarchus; and in many localized dark mantling deposits (LDMDs) (e.g., Gaddis et al., 1985, 2000, 2011; Gustafson et al., 2012; Hawke et al., 2013; Schmitt, personal communication, 2013). Not all of these deposits exhibit uniform spectral features. Schmitt, personal communication (2013) noted red, yellow, orange, and black discolorations associated with the Sulpicius Gallus deposits visible from a 60 km Apollo 17 orbit using a 10× monocular. The low-reflectance deposits at Lassell have *I*/*F* values similar to those of mare, which are not as low in reflectance as most juvenile, glassy RDMDs. However, smaller area DMDs, with large fragmental basaltic plug or wall rock components, have a range of reflectivities between those of mare and highlands (e.g., Hawke et al., 1989; Gaddis et al., 2003).

The relatively thin layer of low-reflectance materials on the massif may thus be a mantling layer, perhaps associated with episodes of mafic eruptions (either from the massif or nearby vents). However, there are considerable differences between typical DMD compositions (mafic) and the *bulk* of the Lassell massif 'red spot' (which is predominantly silicic, Fe-poor, and enriched in Th). Recent work on the Compton–Belkovich Volcanic Complex proposed a highly silicic form of pyroclastic eruption possible for the Moon (Jolliff et al., 2011; Chauhan et al., 2015), although this material is characterized by high reflectance. We suggest that the occurrence of low-reflectance materials at Lassell is consistent with a pyroclastic origin, but sample collection and analysis will be required to make definitive determinations of these and other materials across the massif as their compositions are not resolved by current instruments.

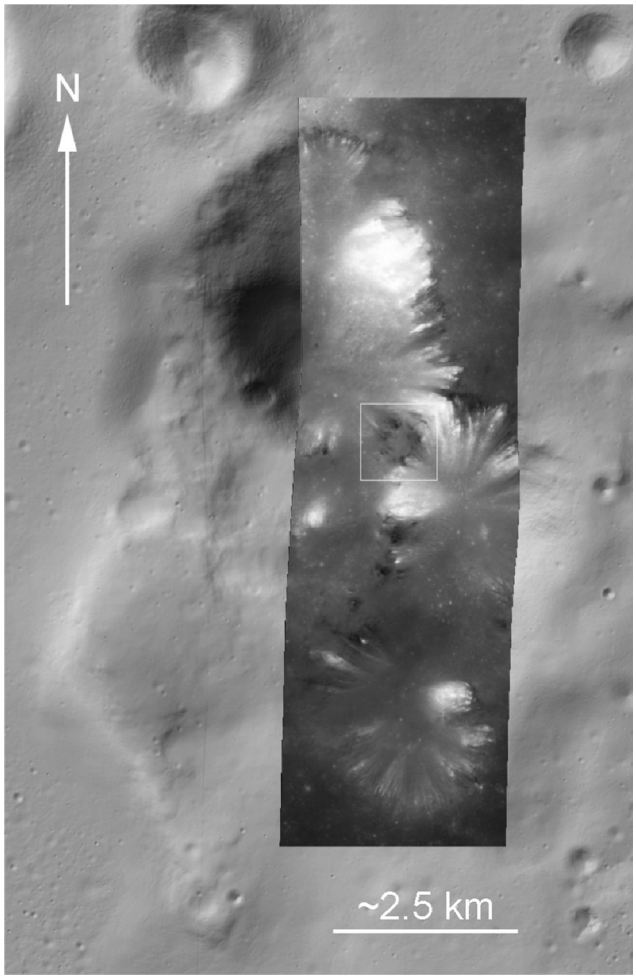

Fig. 13. Low-incidence angle (21°) NAC frame M1116585481R superposed on NAC DTM shaded relief for context. White square shows Fig. 14a location.

The hummocky floor topography of Lassell C crater is thickest along its eastern portion. The Lassell C floor may be blanketed by landslide accumulations, possibly resulting from seismic energy associated with the formation of the younger (fresher), unnamed 2.5-km impact just east of Lassell C (visible in Figs. 1b, 3–5, 7 and 13). However, the maturity of materials in Lassell C is higher than that observed for materials associated with the formation of the small crater to the east, so if a landslide event was responsible for the hummocky deposits, it likely occurred well before the formation of the small crater to the east, making a landslide interpretation associated with this particular crater problematic. Alternatively, given evidence for nearby volcanic activity, the floor of Lassell C may be mantled by pyroclastic materials. The Lassell C floor has FeO, TiO_2, and silica concentrations intermediate to the massif and surrounding mare deposits (Figs. 7 and 8) that could be interpreted as either (1) a mantle of non-mare materials overlying predominantly mare deposits, or (2) evidence for a Fe-bearing pyroclastic mantle over non-mare materials. The second possibility would require source vents somewhere within the nearby portion of the massif. Such vents could be buried, or possibly associated with craters Lassell G and K, which we interpret to be likely vents or collapse calderas.

A range of volcanic mechanisms are theoretically responsible for the silicic massif deposits, and may include basaltic underplating (Hagerty et al., 2006; Glotch et al., 2010), or shallow KREEP-basalt intrusion (e.g., Jolliff et al., 2011), possibly in combination with silicate liquid immiscibility (e.g., Thompson et al., 2007) following fractional crystallization with gravity separation and stratification. However, current understanding of immiscibility dynamics does not account for its occurrence on scales with the volume of the Lassell massif (km^3 scale). Underplating is more efficient at partial melting if the intruded country rock is already differentiated as is, for example, a KREEP-basalt. The massif low-reflectance materials could represent emplacement of late-stage, minor iron-bearing effusive basalts or pyroclastics resulting from magma chamber stratification (e.g., Blake, 1981). The Lassell massif exhibits several similarities with the Compton–Belkovich silicic-volcanic complex (Jolliff et al., 2011; Chauhan et al., 2015) and the Mairan domes (Glotch et al., 2010), including elevated Th concentrations (Hagerty et al., 2006), pits with irregular to arcuate margins, candidate volcanic cones (e.g., Fig. 10), lobate flows, and Si-rich materials. Similar morphologic and geochemical characteristics among well-separated regions imply wide-ranging though isolated operation of Si-rich magmagenesis and silicic volcanism.

5. Conclusions

In summary, Diviner-derived CF values indicative of silicic volcanism correlate spatially with geomorphologic features across the Lassell massif deposits. The highest concentrations of silicic materials occur on the southern massif, centered on the Lassell G and K negative-relief features. This silica-rich zone is also contained within the historic UV-absorbing red spot area. The absence of ejecta blankets and raised rims at Lassell G and K are inconsistent with an impact formation mechanism. Their coalescing character, arcuate margins, and steep interior slopes rather support an explosive volcanic vent complex and/or collapse caldera interpretation involving multiple episodes of collapse.

Sub-kilometer-scale lobate deposits with clear superposition relationships provide a relative timing of deposit emplacement, and suggest that a series of silicic lava flows emanated from the Lassell G and K region. Based on CSFD model age determinations, the massif was emplaced at ~4 Ga, prior to the surrounding mare (3.38 Ga, Hiesinger et al., 2003). Because the CSFD for the smaller crater population runs quasi-parallel to the nominal equilibrium line, the area was likely affected by a long-term, continuous process of resurfacing, such as mass-wasting and/or accumulation of pyroclastic deposits. Possible discrete events at ~900 and ~400 Ma may have resulted from shaking caused by the formation of nearby Copernican craters. The youngest age documented in unit uMc (~60 Ma) likely represents the age of the local regolith.

Relatively low-reflectance deposits exposed by impact craters and mass wasting across the massif also suggest that either pyroclastic materials, minor basaltic extrusions, and/or glassy silicic materials (e.g., obsidian) were emplaced along with the silicic lava flows. Thickening of deposits in eastern Lassell C crater in the direction of Lassell G and K may be the result of (1) landslides from the eastern crater wall, or (2) pyroclastic accumulations having the Lassell massif as the source. These deposits are more intermediate compositionally between mare or other DMD and the Si-rich deposits comprising the massif, so may represent components of both processes.

The Lassell massif, together with features of the surrounding region, indicate a compositionally complex volcanic history for this portion of Mare Nubium. Definitively unraveling the complex geologic history of this region requires future robotic or human exploration focused on mapping contacts and returning soil and rock samples that would provide absolute age dates and major and minor element chemistry determinations.

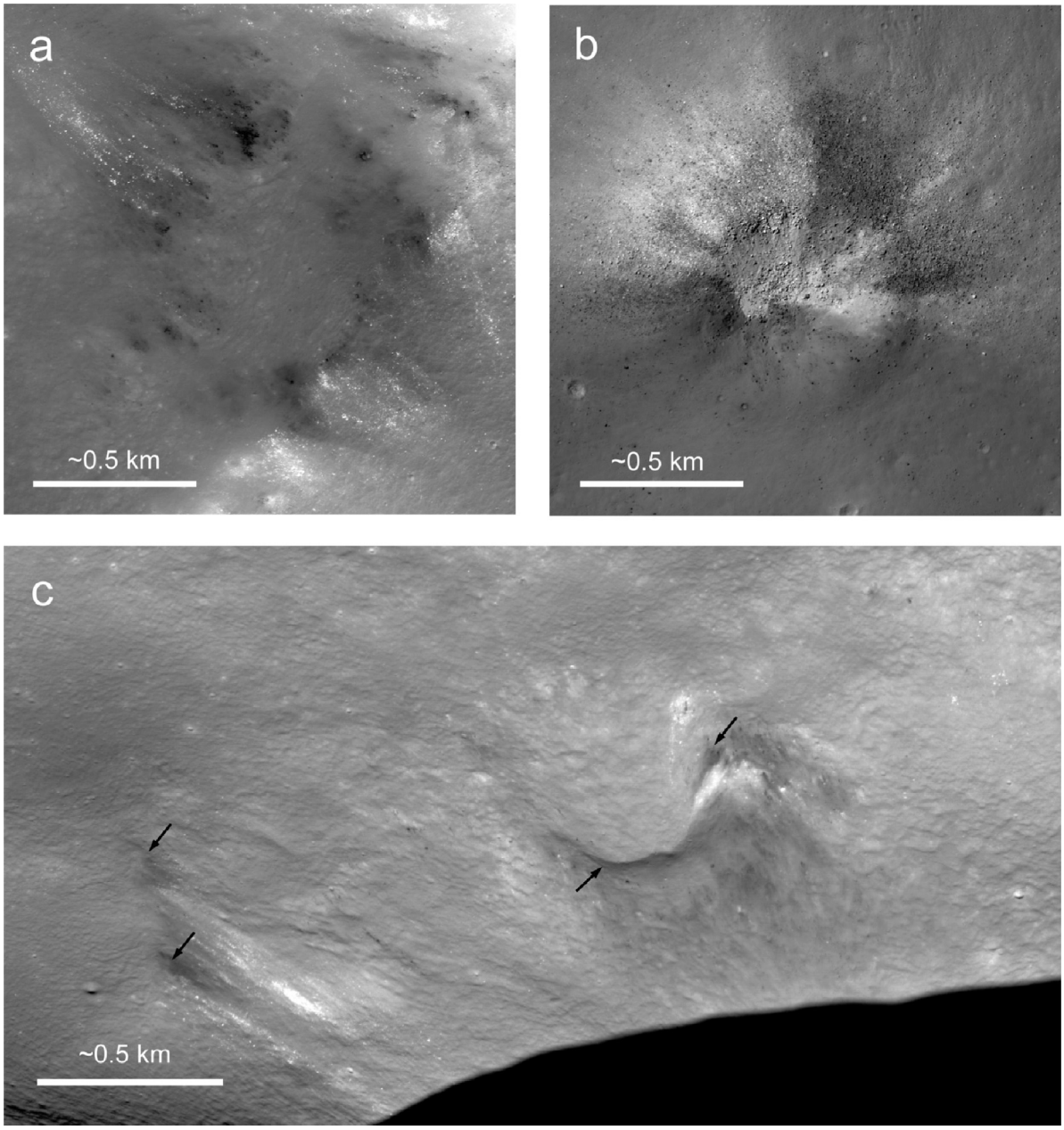

Fig. 14. (a) Low-reflectance deposits between Lassell G and K exposed through mass wasting (white square in Fig. 13). (b) Low-reflectance deposits in the northern uM unit exposed by cratering and impact excavation (NAC M152939732L; location of impact at tip of yellow arrow in Fig. 3). (c) Enlarged portion of NAC oblique frame M1108311369 (also shown in Fig. 3), exhibiting low-reflectance deposits exposed by both impact and mass wasting processes on the western wall of Lassell G.

Acknowledgments

We would like to thank Dr. Debra Hurwitz and Dr. Briony Horgan, who provided insightful reviews. This work was supported by the Lunar Reconnaissance Orbiter Camera (LROC) project. The authors gratefully acknowledge the contributions of the Lunar Reconnaissance Orbiter and LROC Teams. H. Hiesinger and C.H. van der Bogert were funded by the German Space Agency (DLR). The final draft of this paper is submitted in fond memory of co-author Dr. Bernard Ray Hawke.

References

Anderson, J.A. et al., 2004. Modernization of the Integrated Software for Imagers and Spectrometers. Lunar Planet. Sci. 35. Abstract 2039.

Blake, S., 1981. Eruptions from zoned magma chambers. J. Geol. Soc. 138, 281–287. doi:10.1144/gsjgs.138.3.0281.

Braden, S.E., et al., 2014. Evidence for basaltic volcanism on the Moon within the past 100 million years. Nat. Geosci. 7, 787–791. doi:10.1038/NGEO2252.

Bruno, B.C., Lucey, P.G., Hawke, B.R., 1991. High-resolution UV–visible spectroscopy of lunar red spots. Proc. Lunar Sci. Conf. 21, 405–415.

Burns, K.N. et al., 2012. Digital terrain models and derived products from LROC NAC stereo observations. In: XXII Congress of the International Society for Photogrammetry and Remote Sensing, Melbourne, Victoria, Australia (abstract).

Chauhan, M., et al., 2015. Compton–Belkovich Volcanic Complex (CBVC): An ash flow caldera on the Moon. Icarus 253, 115–129. doi:10.1016/j.icarus.2015.02.024.

Chevrel, S.D., Pinet, P.C., Head, J.W., 1999. Gruithuisen domes region: A candidate for an extended nonmare volcanism unit on the Moon. J. Geophys. Res. 104, 16515–16529.

Crater Analysis Techniques Working Group, 1979. Standard techniques for presentation and analysis of crater size-frequency data. Icarus 37, 467–474.

Dundas, C.M., et al., 2010. Role of material properties in the cratering record of young platy-ridged lava on Mars. Geophys. Res. Lett. 37, L12203. doi:10.1029/2010GL042869.

Gaddis, L.R., Pieters, C.M., Hawke, B.R., 1985. Remote sensing of lunar pyroclastic mantling deposits. Icarus 61, 461–489.

Gaddis, L.R., et al., 2000. Compositional analyses of small lunar pyroclastic deposits using Clementine multispectral data. J. Geophys. Res. 105, 4245–4262.
Gaddis, L.R., et al., 2003. Compositional analyses of lunar pyroclastic deposits. Icarus 161, 262–280.
Gaddis, L.R. et al., 2011. Alphonsus dark-halo craters: Identification of additional volcanic vents. Lunar Planet. Sci. 42. Abstract 2691.
Gillis, J.J., Jolliff, B.L., Korotev, R.L., 2004. Lunar surface geochemistry: Global concentrations of Th, K, and FeO as derived from Lunar Prospector and Clementine data. Geochim. Cosmochim. Acta 68, 3791–3805.
Glotch, T.D., et al., 2010. Highly silicic compositions on the Moon. Science 329, 1510–1512.
Glotch, T.D., et al., 2011. The Marian domes: Silicic volcanic constructs on the Moon. Geophys. Res. Lett. 38. doi:10.1029/2011GL049548.
Greeley, R., Batson, R.M., 1990. Planetary Mapping. Cambridge University Press, Cambridge, UK 261pp.
Greenhagen, B.T., et al., 2010. Global silicate mineralogy of the Moon from the Diviner Lunar Radiometer. Science 329, 1507–1509. doi:10.1126/science.1192196.
Gustafson, J.O., et al., 2012. Characterization of previously unidentified lunar pyroclastic deposits using Lunar Reconnaissance Orbiter Camera data. J. Geophys. Res. 117. doi:10.1029/2011JE003893.
Hagerty, J.J., et al., 2006. Refined thorium abundances for lunar red spots: Implications for evolved, nonmare volcanism on the Moon. J. Geophys. Res. 111. doi:10.1029/2005JE002592.
Hartmann, W.K., 1966. Early lunar cratering. Icarus 5, 406–418.
Hawke, B.R., Head III, J.W., 1977. Pre-Imbrian history of the Fra Mauro region and Apollo 14 sample provenance. Proc. Lunar Sci. Conf. 8, 2741–2761.
Hawke, B.R. et al., 1989. Remote sensing and geologic studies of localized dark mantle deposits on the Moon. Proc. Lunar Sci. Conf. 19, 255–268.
Hawke, B.R. et al., 2001. Remote sensing studies of selected spectral anomalies on the Moon. Lunar Planet. Sci. 32. Abstract 1241.
Hawke, B.R., et al., 2003. Hansteen Alpha: A volcanic construct in the lunar highlands. J. Geophys. Res. 108. doi:10.1029/2002JE002013.
Hawke, B.R. et al., 2013. Cryptomare and pyroclastic deposits on the northern east side of the Moon. Lunar Planet. Sci. 44. Abstract 1883.
Head III, J.W., McCord, T.B., 1978. Imbrian-age highland volcanism on the Moon: The Gruithuisen and Mairan domes. Science 199, 1433–1436.
Hiesinger, H., et al., 2000. Ages of mare basalts on the lunar nearside. J. Geophys. Res. 105, 29239–29275.
Hiesinger, H., et al., 2003. Ages and stratigraphy of mare basalts in Oceanus Procellarum, Mare Nubium, Mare Cognitum, and Mare Insularum. J. Geophys. Res. 108. doi:10.1029/2002JE001985.
Jolliff, B.L., et al., 2011. Non-mare silicic volcanism on the lunar farside at Compton–Belkovich. Nat. Geosci. 4. doi:10.1038/NGEO1212.
Jolliff, B.L. et al., 2012. New views of silicic volcanism on the Moon. In: Second Conference on the Lunar Highlands Crust. Abstract 9037.
Kneissl, T., van Gasselt, S., Neukum, G., 2011. Map-projection-independent crater size-frequency determination in GIS environments – New software tool for ArcGIS. Planet. Space Sci. 59, 1243–1254. doi:10.1016/j.pss.2010.03.015.
Kusuma, K.N., Sebastian, N., Murty, S.V.S., 2012. Geochemical and mineralogical analysis of Gruithuisen region on Moon using M3 and DIVINER images. Planet. Space Sci. 67, 46–56.
Lawrence, D.J., et al., 2003. Small-area thorium features on the lunar surface. J. Geophys. Res. 108. doi:10.1029/2003JE002050.
Lawrence, S.J., et al., 2013. LRO observations of morphology and surface roughness of volcanic cones and lobate lava flows in the Marius Hills. J. Geophys. Res. 118. doi:10.1002/jgre.20060.
Lawrence, S.J. et al., 2014. Remote sensing and geologic observations of “red spots” in the Cognitum region. Lunar Planet. Sci. 45. Abstract 2279.
Logan, L.M., et al., 1973. Compositional implications of the Christiansen frequency maximums for infrared remote sensing applications. J. Geophys. Res. 78, 4983–5003.
Lucey, P.G., Blewett, D.T., Jolliff, B.L., 2000a. Lunar iron and titanium abundance algorithms based on final processing of Clementine ultraviolet–visible images. J. Geophys. Res. 105, 20297–20305.
Lucey, P.G., et al., 2000b. Imaging of lunar surface maturity. J. Geophys. Res. 105, 20377–20386.
Mahanti, P., et al., 2014. A standardized approach for quantitative characterization of impact crater topography. Icarus 241, 114–129. doi:10.1016/j.icarus.2014.06.023.
Malin, M.C., 1974. Lunar red spots: Possible pre-mare materials. Earth Planet. Sci. Lett. 21, 331–341.
Melosh, H.J., Ivanov, B.A., 1999. Impact crater collapse. Annu. Rev. Earth Planet. Sci. 27, 385–415.
Michael, G.G., Neukum, G., 2010. Planetary surface dating from crater size-frequency distribution measurements: Partial resurfacing events and statistical age uncertainty. Earth Planet. Sci. Lett. 294, 223–229. doi:10.1016/j.epsl.2009.12.041.
Müller, A., Hawke, B.R., Lucey, P.G., 1986. Remote sensing and geologic studies of the Lassell region of the Moon. Proc. Lunar Sci. Conf. 17, 577–578.
Neukum, G., 1983. Meteoritenbombardement und Datierung planetarer Oberflächen. Habilitation Thesis. Univ. München, Munich, Germany.
Neukum, G., Ivanov, B.A., Hartmann, W.K., 2001. Cratering records in the inner Solar System in relation to the lunar reference system. Space Sci. Rev. 96, 55–86.
Ostrach, L.R. et al., 2011. Effects of incidence angle on crater counting observations. Lunar Planet. Sci. 42, #1202.
Pasckert, J.H., Hiesinger, H., van der Bogert, C.H., 2015. Small-scale lunar farside volcanism. Icarus 257, 336–354. doi:10.1016/j.icarus.2015.04.040.
Pike, R.J., 1977. Apparent depth/apparent diameter relation for lunar craters. Proc. Lunar Sci. Conf. 8, 3427–3436.
Robinson, M.S., et al., 2010. Lunar Reconnaissance Orbiter Camera (LROC) instrument overview. Space Sci. Rev. 150, 81–124.
Salisbury, J.W., et al., 1995. Thermal infrared spectra of the Moon. Icarus 115, 181–190.
Scholten, F., et al., 2012. GLD100: The near-global lunar 100 m raster DTM from LROC WAC stereo image data. J. Geophys. Res. 117. doi:10.1029/2011JE003926.
Schultz, P.H., Greeley, R., Gault, D., 1977. Interpreting statistics of small lunar craters. Proc. Lunar Sci. Conf. 8, 3539–3564.
Soderblom, L.A., 1970. A model for small-impact erosion applied to the lunar surface. J. Geophys. Res. 75, 2655–2661.
Stopar, J.D., et al., 2014a. Occurrence and mechanisms of impact melt emplacement at small lunar craters. Icarus 243, 337–357. doi:10.1016/j.icarus.2014.08.011.
Stopar, J.D. et al., 2014b. Basaltic cones: A relatively common and distinct style of lunar volcanism. Lunar Planet. Sci. 45. Abstract 1425.
Tanaka, K.L., Skinner, J.A., Hare, T.M., 2010. Planetary Geologic Mapping Handbook. U.S. Geological Survey, Astrogeology Science Center, Flagstaff, AZ 21pp.
Thompson, A.B., Aerts, M., Hack, A.C., 2007. Liquid immiscibility in silicate melts and related systems. Rev. Miner. Geochem. 65, 99–127.
Tran, T. et al., 2010. Generating digital terrain models using LROC NAC images. In: International Symposium IV/7 Planetary Mapping and Databases. Institute of Planetary Research, Orlando, FL (abstract).
van der Bogert, C.H. et al., 2015. Development of guidelines for recommended lunar CSFD count area sizes via analysis of random CSFDs. Workshop on Issues in Crater Studies and the Dating of Planetary Surfaces, Laurel, MD, #9023.
Wagner, R., et al., 2010. Lunar red spots: Stratigraphic sequence and ages of domes and plains in the Hansteen and Helmet regions on the lunar nearside. J. Geophys. Res. 115. doi:10.1029/2009JE003359.
Weitz, C.M., Head, J.W., 1999. Spectral properties of the Marius Hills volcanic complex and implications for the formation of lunar domes and cones. J. Geophys. Res. 104, 18933–18956.
Whitaker, E.A., 1972a. Color contrasts in Mare Nubium and the Southern Oceanus Procellarum. Apollo 16 Preliminary Science Report. NASA SP-315, pp. 29-104–129-105.
Whitaker, E.A., 1972b. Lunar color boundaries and their relationship to topographic features: A preliminary survey. The Moon 4, 348–355.
Wilcox, B.B., et al., 2005. Constraints on the depth and variability of the lunar regolith. Meteorit. Planet. Sci. 40, 695–710.
Wilson, L., Head, J.W., 2003. Lunar Gruithuisen and Mairan domes: Rheology and mode of emplacement. J. Geophys. Res. 108. doi:10.1029/2002JE001909.
Wilson, J.T. et al., 2015. Evidence for explosive silicic volcanism on the Moon from the extended distribution of thorium near the Compton–Belkovich Volcanic Complex. Lunar Planet. Sci. 46. Abstract 2081.
Wood, C.A., 1979. Monogenetic volcanoes of the terrestrial planets. Proc. Lunar Sci. Conf. 10, 2815–2840.
Wood, C.A., Head III, J.W., 1975. Geologic setting and provenance of spectrally distinct pre-mare material of possible volcanic origin. In: Conference on Origins of Mare Basalts. Lunar and Planetary Institute, Houston, TX, pp. 189–193.
Young, R.A., 1975. Mare crater size-frequency distributions: Implications for relative surface ages and regolith development. Proc. Lunar Sci. Conf. 6, 2645–2662.